Available online at www.sciencedirect.com
SCIENCE DIRECT®
Finite Elements in Analysis and Design 40 (2004) 2063–2084
FINITE ELEMENTS IN ANALYSIS AND DESIGN
www.elsevier.com/locate/finel

Local absorbing boundaries of elliptical shape for scalar wave propagation in a half-plane

Sanghoon Lee[a], Loukas F. Kallivokas[a,b,*]

[a] *Department of Civil Engineering, The University of Texas at Austin, 1 University Station C1748, Austin, TX 78712, USA*

[b] *Institute for Computational Engineering and Sciences, The University of Texas at Austin, USA*

Received 1 September 2003; accepted 15 February 2004

Abstract

We have recently discussed the performance of local second-order two-dimensional absorbing boundary conditions of elliptical shape for scattering and radiation problems involving sound-hard obstacles embedded in a full-plane. In this article, using the method of images, we extend the applicability of elliptically shaped truncation boundaries to semi-infinite acoustic media. For problems in either the time- or the frequency-domains, involving near-surface structures of elongated cross-sections, we show that significant computational savings are attainable when compared against semi-circular truncation geometries.

Keywords: Absorbing boundary conditions; Half-space or half-plane; Scalar wave equation; Elliptical shape; Time-domain; Frequency-domain

1. Introduction

When domain discretization methods are used in the numerical simulation of acoustic waves in unbounded domains, whether of infinite or semi-infinite extent, there always arises the need to truncate the unbounded domain to a finite computational one. The truncation is achieved through the introduction of an artificial boundary that limits the extent of the unbounded domain. For well-posedness of the ensuing initial-and-boundary-value problem (IBVP) over the finite domain, an appropriate (absorbing, silent, artificial, etc.) condition need also be prescribed on the truncation boundary. Typically, it is difficult to obtain an *exact* absorbing condition for *arbitrary* truncation geometries (if it

* Corresponding author. Department of Civil Engineering, The University of Texas at Austin, 1 University Station C1748, Austin, TX 78712, USA. Tel.: +1-512-232-5769; fax: +1-512-471-7259.
E-mail addresses: sang@mail.utexas.edu (S. Lee), loukas@mail.utexas.edu (L.F. Kallivokas).

0168-874X/$ - see front matter © 2004 Elsevier B.V. All rights reserved.
doi:10.1016/j.finel.2004.02.005

at all exists). Such an exact condition can be seen as a near-field instantiation of the Sommerfeld radiation condition—realized closer to the origin rather than at infinity.

Exact conditions on truncation boundaries are referred to as DtN (Dirichlet-to-Neumann) maps, for they typically relate the Dirichlet to the Neumann datum on the boundary [1,2]. DtN conditions are, by construction, spatially and temporally non-local, even for the few canonical geometries for which the apparatus of separation of variables allows for their construction. The non-locality of DtN maps imposes onerous computational requirements. By contrast, and in order to overcome the exact condition's difficulties, local approximants in both time and space of the DtN maps offer the benefit of reduced computational cost at the expense of accuracy. Oftentimes, but not always, the trade-off is user-controllable, via: (a) the order of the local approximant (increasing orders lead to increased spatial and temporal coupling); and (b) the location of the truncation boundary (the farther the boundary is placed, the fewer the reflections are).

For the computational benefits they afford, it is without surprise that a significant amount of work has been devoted to devising local constructs of the truncation condition. Extensive surveys, both early and recent, of developments in this area include the works in [2–6]. Local constructs can be roughly classified in two categories: those based on rational approximations of the dispersion relation, and those based on asymptotic expansions of the far-field solution or the solution exterior to the computational domain. As examples, we mention here the pioneering works of Engquist and Majda [7,8], and Bayliss and Turkel [9–11]. Most of these and related works, however, were limited to canonical geometries (straight, circular, or spherical boundaries). It is conceivable though that other geometries may offer computational advantages, especially in the presence of elongated scatterers. However, numerical results pertaining to non-circular or non-spherical geometries are scant.

For example, in the context of two-dimensional elliptically shaped local boundaries we mention ad hoc (as opposed to systematic) developments [12–17] largely based on generalizations of the Bayliss–Turkel conditions to elliptical or general convex geometries without, however, the benefit of generalization to higher-order conditions, and the systematic works of Grote and Keller [18], Antoine et al. [19], Barry et al. [20], and Kallivokas et al. [21–23]. Finite element implementations of up to second-order conditions have recently appeared for elliptical and arbitrarily shaped geometries [24,25] for frequency-domain applications only, whereas comparisons of elliptical boundary developments up to 1996 have also been reported [26,27].

The works discussed thus far pertain mostly to the full-plane or full-space case. In [28], we showed how a family of absorbing boundary conditions prescribed on arbitrarily-convex truncation surfaces (three-dimensional case) can be applied to the half-space problem; therein, numerical results were presented for semi-spherical truncation boundaries endowed with second-order conditions. To the best of our knowledge, local absorbing conditions applicable to both time- and frequency-domain problems for half-plane problems prescribed on non-circular boundaries have not appeared. Thus, this paper fills this gap by extending past work [29,28], most notably the approach followed for the half-space three-dimensional case [28]; herein, we present numerical results for elliptically-shaped boundaries for the half-plane case in both the frequency- and time-domains using a local second-order absorbing boundary condition.

The rest of the article is organized as follows: we treat first the continuous problem starting with the full-plane setting, and repeat the main theoretical results from recent work [30]; using the full-plane development, we particularize next the conditions to the half-plane case and provide the framework for resolving the waves in the semi-infinite medium using the method of images. In the numerical

section we present results pertaining to both canonical and arbitrary scatterers using both elliptically shaped and circular truncation geometries for applications in the time- and frequency-domains and establish the computational advantages elliptically shaped boundaries offer. Lastly, in Appendix A, we provide an exact solution to a prototype problem involving cylindrical obstacles, which is used to compare against the numerical results.

2. The continuous problem

2.1. Propagation in full-plane

We consider first the exterior problem in a full-plane governed by the time-dependent wave equation. Let Γ be a closed curve with exterior $\Omega \subset \Re^2$; Ω is occupied by a linear, inviscid, and compressible fluid. Without loss of generality we focus on the scattering problem in which a traveling plane wave p^0 impinges upon a rigid structure [1] (Fig. 1a), and seek to determine the scattered (or total) pressure field within Ω. [2] The strong form of the problem can be stated as

Given $p^0(\boldsymbol{x},t)$ with $\boldsymbol{x} \in \Omega$, find $p(\boldsymbol{x},t)$ such that

$$\ddot{p}(\boldsymbol{x},t) = c^2 \Delta p(\boldsymbol{x},t), \quad \boldsymbol{x} \in \Omega, \ t > 0, \tag{1}$$

$$p_\nu(\boldsymbol{x},t) + p^0_\nu(\boldsymbol{x},t) = 0, \quad \boldsymbol{x} \in \Gamma, \ t > 0, \tag{2}$$

$$\lim_{r\to\infty} \sqrt{r}\left(p_r + \frac{1}{c}\dot{p}\right) = 0, \tag{3}$$

$$p(\boldsymbol{x},0) = 0, \quad \dot{p}(\boldsymbol{x},0) = 0, \quad \boldsymbol{x} \in \bar{\Omega}, \tag{4}$$

where p denotes scattered pressure, $\boldsymbol{x}$ is the position vector, t is time, ν is the outward unit normal on Γ, c is the velocity of wave propagation, Δ is the Laplace operator, an overdot denotes derivative with respect to time, and p_ν denotes the normal derivative of the scattered pressure p. Condition (2) implies that the normal fluid acceleration vanishes on the boundary of the scatterer, or equivalently, that the normal derivative of the total pressure also vanishes on Γ. Condition (3), in which r is radial distance and p_r the derivative of the pressure along the radial direction, is the Sommerfeld radiation condition. Condition (4) indicates that the system is taken to be initially at rest.

Following classical lines for resolving unbounded domain problems, the exterior infinite region Ω is truncated via the introduction of an artificial boundary Γ_a. The process gives rise to the finite computational domain Ω_f (Fig. 1b). For well-posedness of the associated IBVP over the finite Ω_f, a boundary condition need also be prescribed on the truncation boundary Γ_a. This condition, which can be determined in terms of the actual solution p on Γ_a, admits the form [23]:

$$p_\nu(\boldsymbol{x},t) = \mathscr{F}[p^t(\cdot,\cdot)](\boldsymbol{x}), \quad \boldsymbol{x} \in \Gamma_a, \tag{5}$$

in which the dots following p^t indicate dummy variables, and $\mathscr{F}$ is an integral operator that depends on p^t, the time history of p, i.e.,

$$p^t(t) = p(t-\tau), \forall\tau\colon\ 0 \leqslant \tau \leqslant t. \tag{6}$$

[1] Throughout this article, the scatterer is considered to be immobile.

[2] Radiation problems can be similarly treated.

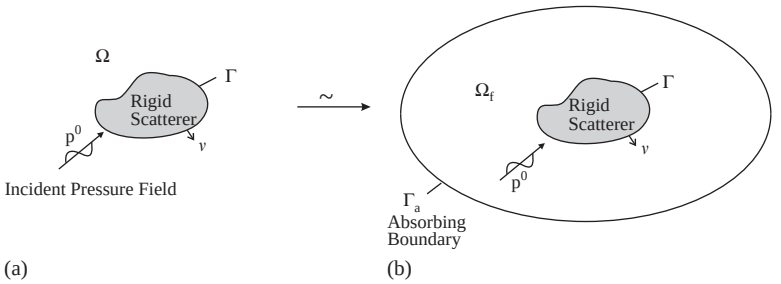

Fig. 1. (a) Exterior scattering problem in unbounded full-plane; and (b) reduced model with finite fluid region Ω_f and artificial boundary Γ_a.

$\mathscr{F}$ is non-local in time and space, that is to say, the motion at any given instant t at every point on the artificial boundary Γ_a is coupled with the time histories of all other points on Γ_a. The non-local character of the exact $\mathscr{F}$ makes it unsuitable for implementation in the context of domain discretization methods. In [21], we developed a family of localized approximants to $\mathscr{F}$ for arbitrarily convex truncation boundaries and have used its members in applications implicating circular truncation boundaries in a full-plane. Recently, in [30], we presented numerical results for elliptically shaped boundaries also in a full-plane. Here, we use a second-order approximant to $\mathscr{F}$, denoted by $\mathscr{F}_2$, prescribed on an elliptical boundary for half-plane applications; this local second-order condition is particularly well-suited for numerical implementation using finite elements. In the next section, we discuss the essential theoretical results from [30] that lead to the second-order approximant. We remark that, with the introduction of the artificial boundary and the approximant $\mathscr{F}_2$, the IBVP (1)–(4) is now replaced by

$$\ddot{p}(\boldsymbol{x},t) = c^2 \Delta p(\boldsymbol{x},t), \quad \boldsymbol{x} \in \Omega_f, \ t > 0, \tag{7}$$

$$p_\nu(\boldsymbol{x},t) = -p_\nu^0(\boldsymbol{x},t), \quad \boldsymbol{x} \in \Gamma, \ t > 0, \tag{8}$$

$$p_\nu(\boldsymbol{x},t) = \mathscr{F}_2[p(\boldsymbol{x},t)], \quad \boldsymbol{x} \in \Gamma_a, \ t > 0, \tag{9}$$

$$p(\boldsymbol{x},0) = 0, \quad \dot{p}(\boldsymbol{x},0) = 0, \quad \boldsymbol{x} \in \bar{\Omega}_f. \tag{10}$$

2.2. The absorbing boundary

Let Γ_a (the absorbing boundary) be smooth and convex and let it be described by the parametric representation $\boldsymbol{X}(\lambda)$, where $\boldsymbol{X}$ denotes the position vector on Γ_a, and λ is an arc-length parameter (Fig. 2). Using a Fermi-type coordinate system, it can be shown [30,20,21] that a second-order absorbing boundary condition on Γ_a is given by

$$\dot{p}_\nu + \gamma p_\nu = -\frac{1}{c}\ddot{p} + \left(\frac{1}{2}\kappa - \frac{\gamma}{c}\right)\dot{p} + \frac{1}{2}c\,p_{\lambda\lambda} + \left(\frac{1}{8}\kappa^2 c + \frac{1}{2}\kappa\gamma\right)p, \tag{11}$$

where γ is an arbitrary non-negative parameter, and κ denotes the curvature of Γ_a (for convex Γ_a, $\kappa(\boldsymbol{x}) < 0, \forall \boldsymbol{x} \in \Gamma_a$).

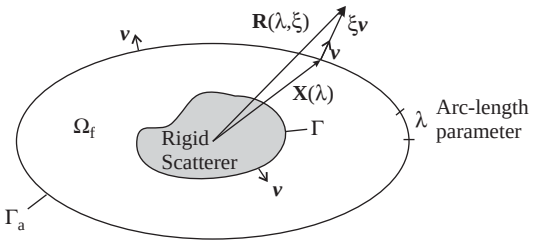

Fig. 2. Artificial boundary Γ_a in a Fermi-type coordinate system characterized by the planar curve parameter λ and scalar distance metric ξ.

The parameter γ in (11) has been formally introduced for stability in time-domain applications. Specifically, in [30] we derived (11) (and all members of the family of approximants) using asymptotic expansions, in the Laplace transform domain, of the solution to the problem exterior to Γ_a. The parameter γ was introduced into these expansions to ensure the stability of the solution when the expansions are transformed back to the time-domain. From a physical point of view, γ represents damping introduced through the boundary Γ_a. In [20,21], it was shown that, to ensure the dissipativity of the conditions, γ need be greater than a critical value above which exponential error growth in time-domain applications is prevented. In [30], for elliptically shaped boundaries, we used:

$$\gamma(\boldsymbol{x}) = -c\kappa(\boldsymbol{x}). \tag{12}$$

With choice (12), the second-order condition (11) becomes

$$\dot{p}_\nu - c\kappa p_\nu = -\frac{1}{c}\,\ddot{p} + \frac{3}{2}\,\kappa\dot{p} + \frac{1}{2}\,c\,p_{\lambda\lambda} - \frac{3}{8}\,\kappa^2 c\,p. \tag{13}$$

It can be easily verified that either (11) or (13) cannot be readily incorporated into a weak form tantamount to the strong statement of the modified IBVP (7)–(10), since (11) or (13) contain both the normal derivative p_ν and its first time derivative, i.e., $\dot{p}_\nu$. To do this efficiently, we introduce two auxiliary variables on the artificial boundary, $q^{(1)}$ and $q^{(2)}$, and decompose (13) into the following equivalent set of three equations:

$$-p_\nu = \frac{1}{c}\,\dot{p} - \frac{1}{2}\,\kappa p - \frac{c}{2}\,q^{(1)}_{\lambda\lambda} - \frac{c}{8}\,\kappa^2 q^{(2)}, \tag{14}$$

$$p_{\lambda\lambda} - \dot{q}^{(1)}_{\lambda\lambda} + c\kappa q^{(1)}_{\lambda\lambda} = 0, \tag{15}$$

$$p - \dot{q}^{(2)} + c\kappa q^{(2)} = 0. \tag{16}$$

Eqs. (14)–(16) allow now the ready incorporation of the second-order condition into a variational statement for the IBVP (7)–(10), at the minimal expense of two additional variables on the absorbing boundary.

2.3. Propagation in a half-plane

We consider next the half-plane propagation problem, and in particular the scattering problem that arises when a traveling wave p_{inc} impinges upon a submerged near-surface object (Fig. 3).

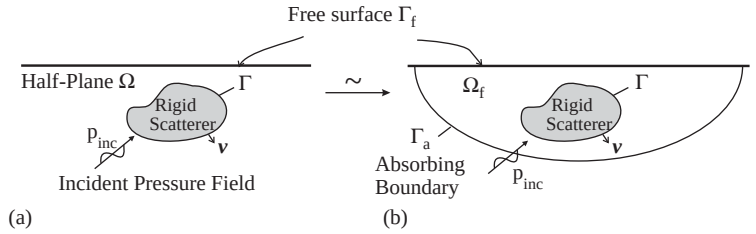

Fig. 3. (a) Exterior scattering problem in a half-plane; and (b) reduced model with finite fluid region Ω_f, artificial boundary Γ_a, and free surface Γ_f.

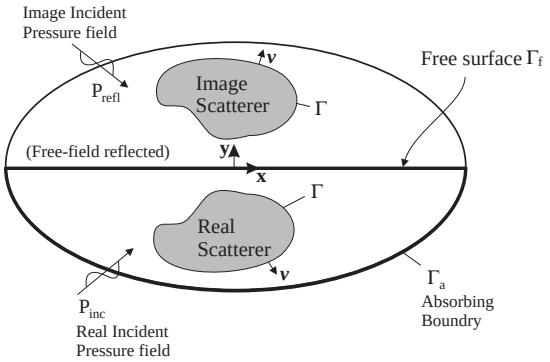

Fig. 4. Method of images: full-plane problem adjoint to the half-plane problem shown in Fig. 3b.

Typically, in full-plane problems, one need only be concerned with the motion within the finite fluid domain: it is expected that the artificial boundary will resolve any outgoing waves to the degree allowed by the order of the approximant to the exact truncation condition (second order here). By contrast, in half-plane scattering problems where full-plane absorbing boundary conditions are used, the introduction of an artificial boundary might give rise to additional errors, particularly in regions close to the intersection of the artificial boundary with the free surface. This is especially true if one were to solve for the scattered wavefield in a manner identical to that of the preceding section (the scattered wavefield on the free surface is non-zero). The peculiarity of the half-plane problem stems from the presence of a free surface which the absorbing boundary conditions, developed originally for full-plane problems, do not readily account for.

To overcome the difficulty imposed by our desire to use full-plane conditions in half-plane problems, we resort to the method of images in order to: (a) ensure the appropriateness of the use of the full-plane condition (13); and (b) ensure that the wavefield one needs to solve for remains zero at all times on the free surface. To this end, we consider the half-plane problem depicted in Fig. 3(b) and its adjoint full-plane problem depicted in Fig. 4. In the latter figure, p_{refl} represents the image incident field of the incident pressure field p_{inc} in the positive half-plane ($y > 0$). In other words, in the negative half-plane p_{refl} represents the free-field reflected wavefield, i.e., the wavefield generated when p_{inc} impinges on the free-surface in the absence of any scatterers. We remark that we require that the free surface be an axis of symmetry of the convex planar region bounded by

the (closed-curve) artificial boundary Γ_a. Having turned our attention to the half-plane problem, henceforth Γ_a is used to denote the (open-curve) artificial boundary in the negative half-plane only (Fig. 4).

Let us define the image incident pressure field as

$$p_{\text{refl}}(x, y, t) = -p_{\text{inc}}(x, -y, t), \quad \forall y. \tag{17}$$

The total pressure field is

$$p_{\text{tot}}(x, y, t) = p^0(x, y, t) + p(x, y, t), \quad \forall y, \tag{18}$$

where p denotes part of the scattered field, and

$$p^0(x, y, t) = p_{\text{inc}}(x, y, t) + p_{\text{refl}}(x, y, t), \quad \forall y. \tag{19}$$

On account of symmetry,

$$p_{\text{tot}}(x, y, t) = -p_{\text{tot}}(x, -y, t), \quad \forall y. \tag{20}$$

Therefore, on the free surface $\Gamma_f(y = 0)$, one has

$$p_{\text{tot}}(x, 0, t) = 0, \tag{21}$$

and from (17)

$$p_{\text{inc}}(x, 0, t) + p_{\text{refl}}(x, 0, t) = 0. \tag{22}$$

Clearly, from (19) and (22), there holds on the free-surface $\Gamma_f(y = 0)$:

$$p^0(x, 0, t) = p_{\text{inc}}(x, 0, t) + p_{\text{refl}}(x, 0, t) = 0. \tag{23}$$

Thus, p^0 above denotes the total free-field wavefield that would have been generated in the absence of any scatterers. p in (18) denotes a scattered pressure wavefield; in physical terms, p is equal to the sum of the scattered fields generated by the real and image scatterers when they are insonified by p_{inc} and p_{refl}, respectively. With these definitions, p is equal to the part of the scattered field understood as the total wavefield less the free-field wave p^0. Notice that by virtue of (18), (21), and (23), there also holds on Γ_f

$$p(x, 0, t) = p_{\text{tot}}(x, 0, t) - p^0(x, 0, t) = 0. \tag{24}$$

We remark that the total scattered wavefield p_{sc} generated in the negative half-plane when p_{inc} impinges on the scatterer is given by

$$p_{\text{sc}}(x, y, t) = p(x, y, t) + p_{\text{refl}}(x, y, t), \forall y \leqslant 0. \tag{25}$$

It can be easily seen now that the adjoint problems (Figs. 3(b) and 4) are equivalent, provided that in the half-plane case one solves for the scattered wavefield p, prescribes (24) on the free surface, and uses p^0 (19) as the excitation. These observations, together with the fact that the right-hand side of the absorbing boundary condition (13) is an odd function with respect to the y coordinate, allow for the ready use of the full-plane condition (13) in the half-plane problem without any modification, i.e., one needs to pose the problem for p only over the lower half-plane in Fig. 4, while prescribing (13) on the restriction of the full-plane artificial boundary in the half-plane. The associated strong form can be cast as

Given an incident field $p_{\text{inc}}(\boldsymbol{x},t)$ with $\boldsymbol{x}\in\Omega_{\text{f}}$ (Fig. 4), find $p(\boldsymbol{x},t)$ such that

$$\ddot{p}(\boldsymbol{x},t)=c^2\Delta p(\boldsymbol{x},t),\quad \boldsymbol{x}\in\Omega_{\text{f}},\ t>0, \tag{26}$$

$$p_v(\boldsymbol{x},t)=-p_v^0(\boldsymbol{x},t)=-\frac{\partial p_{\text{inc}}(\boldsymbol{x},t)}{\partial v}-\frac{\partial p_{\text{refl}}(\boldsymbol{x},t)}{\partial v},\quad \boldsymbol{x}\in\Gamma,\ t>0, \tag{27}$$

$$\begin{aligned}-p_v(\boldsymbol{x},t)&=\frac{1}{c}\dot{p}(\boldsymbol{x},t)-\frac{1}{2}\kappa(\boldsymbol{x})p(\boldsymbol{x},t)-\frac{c}{2}q_{\lambda\lambda}^{(1)}(\boldsymbol{x},t)\\&\quad-\frac{c}{8}\kappa^2(\boldsymbol{x})q^{(2)}(\boldsymbol{x},t),\quad \boldsymbol{x}\in\Gamma_{\text{a}},\ t>0,\end{aligned} \tag{28}$$

$$p_{\lambda\lambda}(\boldsymbol{x},t)-\dot{q}_{\lambda\lambda}^{(1)}(\boldsymbol{x},t)+c\kappa(\boldsymbol{x})q_{\lambda\lambda}^{(1)}(\boldsymbol{x},t)=0,\quad \boldsymbol{x}\in\Gamma_{\text{a}},\ t>0, \tag{29}$$

$$p(\boldsymbol{x},t)-\dot{q}^{(2)}(\boldsymbol{x},t)+c\kappa(\boldsymbol{x})q^{(2)}(\boldsymbol{x},t)=0,\quad \boldsymbol{x}\in\Gamma_{\text{a}},\ t>0, \tag{30}$$

$$p(\boldsymbol{x},0)=0,\quad \dot{p}(\boldsymbol{x},0)=0,\quad \boldsymbol{x}\in\bar{\Omega}_{\text{f}}. \tag{31}$$

3. The discrete problem

3.1. Finite elements

Following classical lines the weak form corresponding to (26)–(31) can be easily shown to be

$$\begin{aligned}&\frac{1}{c^2}\int_{\Omega_{\text{f}}}\delta p\,\ddot{p}\,\mathrm{d}\Omega_{\text{f}}+\int_{\Omega_{\text{f}}}\nabla\delta p\cdot\nabla p\,\mathrm{d}\Omega_{\text{f}}+\frac{1}{c}\int_{\Gamma_{\text{a}}}\delta p\,\dot{p}\,\mathrm{d}\Gamma_{\text{a}}-\frac{1}{2}\int_{\Gamma_{\text{a}}}\kappa\delta p\,p\,\mathrm{d}\Gamma_{\text{a}}\\&\quad+\frac{c}{2}\int_{\Gamma_{\text{a}}}\delta p_\lambda q_\lambda^{(1)}\,\mathrm{d}\Gamma_{\text{a}}-\frac{c}{8}\int_{\Gamma_{\text{a}}}\kappa^2\delta p q^{(2)}\,\mathrm{d}\Gamma_{\text{a}}\\&\quad+\frac{c}{2}\int_{\Gamma_{\text{a}}}\delta q_\lambda^{(1)}\,p_\lambda\,\mathrm{d}\Gamma_{\text{a}}-\frac{c}{2}\int_{\Gamma_{\text{a}}}\delta q_\lambda^{(1)}\,\dot{q}_\lambda^{(1)}\,\mathrm{d}\Gamma_{\text{a}}+\frac{c^2}{2}\int_{\Gamma_{\text{a}}}\kappa\delta q_\lambda^{(1)}\,q_\lambda^{(1)}\,\mathrm{d}\Gamma_{\text{a}}\\&\quad-\frac{c}{8}\int_{\Gamma_{\text{a}}}\kappa^2\delta q^{(2)}\,p\,\Gamma_{\text{a}}+\frac{c}{8}\int_{\Gamma_{\text{a}}}\kappa^2\delta q^{(2)}\,\dot{q}^{(2)}\,\mathrm{d}\Gamma_{\text{a}}-\frac{c}{8}\int_{\Gamma_{\text{a}}}\kappa^3\delta q^{(2)}\,q^{(2)}\,\mathrm{d}\Gamma_{\text{a}}\\&=\int_{\Gamma}\delta p\,p_v^0\,\mathrm{d}\Gamma_{\text{a}}.\end{aligned} \tag{32}$$

The semi-discretized equations corresponding to the variational form (32) can be obtained readily by using standard piecewise polynomials to represent the test and trial functions implicated in (32) (details were given in [30]). The resulting ordinary differential equations have the following second-order structure:

$$\boldsymbol{M}\ddot{\boldsymbol{U}}+\boldsymbol{C}\dot{\boldsymbol{U}}+\boldsymbol{K}\boldsymbol{U}=\boldsymbol{F}, \tag{33}$$

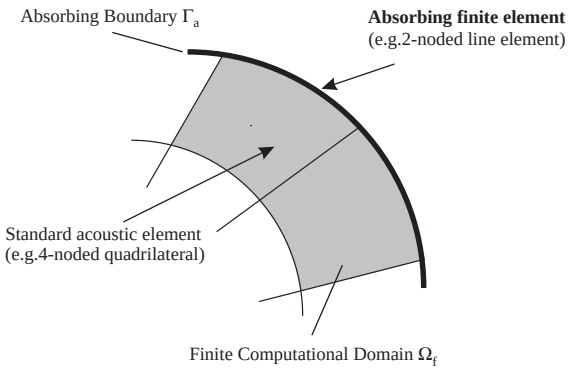

Fig. 5. Representation of the absorbing boundary element.

where

$$\boldsymbol{M} = \begin{bmatrix} \boldsymbol{M}_{p_\Gamma p_\Gamma} & \boldsymbol{M}_{p_\Gamma p_{\Omega_f}} & \boldsymbol{0} \\ \boldsymbol{M}_{p_{\Omega_f} p_\Gamma} & \boldsymbol{M}_{p_{\Omega_f} p_{\Omega_f}} & \boldsymbol{M}_{p_{\Omega_f} p_{\Gamma_a}} \\ \boldsymbol{0} & \boldsymbol{M}_{p_{\Gamma_a} p_{\Omega_f}} & \boldsymbol{M}_{p_{\Gamma_a} p_{\Gamma_a}} \end{bmatrix}, \tag{34}$$

$$\boldsymbol{C} = \begin{bmatrix} \boldsymbol{0} & \boldsymbol{0} & \boldsymbol{0} \\ \boldsymbol{0} & \boldsymbol{0} & \boldsymbol{0} \\ \boldsymbol{0} & \boldsymbol{0} & \boldsymbol{C}^a \end{bmatrix}, \quad \boldsymbol{K} = \begin{bmatrix} \boldsymbol{K}_{p_\Gamma p_\Gamma} & \boldsymbol{K}_{p_\Gamma p_{\Omega_f}} & \boldsymbol{0} \\ \boldsymbol{K}_{p_{\Omega_f} p_\Gamma} & \boldsymbol{K}_{p_{\Omega_f} p_{\Omega_f}} & \boldsymbol{K}_{p_{\Omega_f} p_{\Gamma_a}} \\ \boldsymbol{0} & \boldsymbol{K}_{p_{\Gamma_a} p_{\Omega_f}} & \boldsymbol{K}_{p_{\Gamma_a} p_{\Gamma_a}} + \boldsymbol{K}^a \end{bmatrix}. \tag{35}$$

$\boldsymbol{U}$ is the vector of the unknown nodal quantities, i.e.

$$\boldsymbol{U}^T = [\boldsymbol{p}_\Gamma^T, \quad \boldsymbol{p}_{\Omega_f}^T, \quad \bar{\boldsymbol{p}}_{\Gamma_a}^T] \tag{36}$$

and

$$\boldsymbol{F}^T = [\boldsymbol{f}_{p_\Gamma}^T, \quad \boldsymbol{0}^T, \quad \boldsymbol{0}^T]. \tag{37}$$

In the above, $\bar{\boldsymbol{p}}_{\Gamma_a}^T = [\boldsymbol{p}_{\Gamma_a}^T, \boldsymbol{q}^{(1)^T}_{\Gamma_a}, \boldsymbol{q}^{(2)^T}_{\Gamma_a}]$, $\boldsymbol{f}_{p_\Gamma}$ is the discretized form of the right-hand side of (32), and $\boldsymbol{p}_\Gamma^T$, $\boldsymbol{p}_{\Omega_f}^T$, $\boldsymbol{p}_{\Gamma_a}^T$ denote partitions of p over Γ, Ω_f, and Γ_a, respectively. Notice that the contributions of the absorbing boundary enter through the bottom right blocks in the damping and stiffness matrices (35).

For completeness, we repeat the expressions given in [30,21], that characterize the contributions of the absorbing boundary. As it can be seen from the weak form (32) or the global matrices (35), the contributions of the absorbing boundary give rise to a boundary-only element (Fig. 5) that is completely characterized by the damping and stiffness matrices $\boldsymbol{C}^a$ and $\boldsymbol{K}^a$; the corresponding

element matrices are given as

$$\boldsymbol{k}^{\mathrm{a}} = \begin{bmatrix} -\frac{1}{2}\int_e \kappa\,\psi\,\psi^{\mathrm{T}} & \frac{c}{2}\int_e \psi_{,\lambda}\psi_{,\lambda}^{\mathrm{T}} & -\frac{c}{8}\int_e \kappa^2\,\psi\,\psi^{\mathrm{T}} \\ \frac{c}{2}\int_e \psi_{,\lambda}\psi_{,\lambda}^{\mathrm{T}} & \frac{c^2}{2}\int_e \kappa\psi_{,\lambda}\psi_{,\lambda}^{\mathrm{T}} & 0 \\ -\frac{c}{8}\int_e \kappa^2\,\psi\,\psi^{\mathrm{T}} & 0 & -\frac{c^2}{8}\int_e \kappa^3\,\psi\,\psi^{\mathrm{T}} \end{bmatrix}, \tag{38}$$

$$\boldsymbol{c}^{\mathrm{a}} = \begin{bmatrix} \frac{1}{c}\int_e \psi\,\psi^{\mathrm{T}} & 0 & 0 \\ 0 & -\frac{c}{2}\int_e \psi_{,\lambda}\psi_{,\lambda}^{\mathrm{T}} & 0 \\ 0 & 0 & \frac{c}{8}\int_e \kappa^2\,\psi\,\psi^{\mathrm{T}} \end{bmatrix}. \tag{39}$$

ψ and $\psi_{,\lambda}$ above are the shape functions and their tangential derivatives, respectively (details on the shape functions are provided in Appendix B). The subscript e denotes a line element on the truncation boundary Γ_{a}, and the line differential ($\mathrm{d}\Gamma_{\mathrm{a}}^e$) has been dropped throughout for brevity. We remark that one need only mesh the finite region Ω_{f} and simply attach the absorbing element on the boundary Γ_{a} without any further discretization within the infinite exterior region. Notice that all matrices are frequency-independent and symmetric, thus readily allowing for applications in either the time- or frequency-domain, while maintaining the overall symmetry of the algebraic systems resulting from the discretization of the interior computational domain.

4. Numerical results

Two types of rigid scatterers submerged in a half-plane at different depths of immersion are considered; a circular cylindrical, and a cigar-shaped scatterer. We consider insonification by both time-harmonic and transient plane waves. Numerical results are obtained using the second-order absorbing boundary condition prescribed on both semi-circularly- and semi-elliptically-shaped boundaries. All subsequent references to scattered pressure pertain to the partial scattered field obtained as a solution to (33); to recover the total scattered field one need only add p_{refl} (see A.2).

4.1. Cylindrical scatterer

The geometry of the problem is depicted in Fig. 6; we denote the major semi-axis of the semi-elliptical boundary with s_{M}, the minor semi-axis with s_{m}, and their ratio with $\eta = s_{\mathrm{M}}/s_{\mathrm{m}}$. The cylindrical scatterer has a radius of a. In all cases, the mesh density is kept the same; it is characterized by a typical element size metric of $0.02a$. For the time-harmonic cases we use a frequency sweep between $ka = 0.1$ and $ka = 10$ (low to medium range). With these choices the smallest wavelength is $0.6a$; Therefore, for the highest frequency we consider, the mesh density results in roughly 30 points per wavelength—more than enough to resolve locally the waves. We use linear

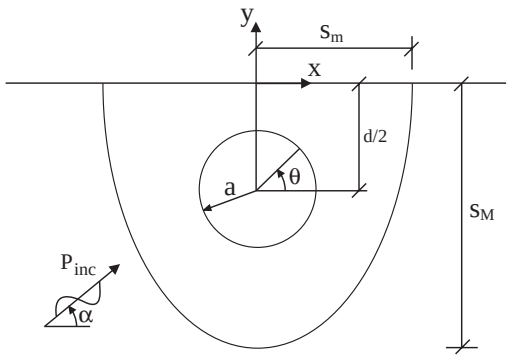

Fig. 6. Model of a rigid circular scatterer in a half-plane surrounded by a semi-elliptical absorbing boundary.

Table 1
Computational cost in terms of the total number of degrees-of-freedom per case for the circular cylindrical scatterer

s_M	Total DOF		$d/2a$
	$\eta = 1$	$\eta = 2$	
4.0a	57,850	23,554	2.0
3.0a	28,658	10,400	1.2
3.0a	28,058	10,248	1.5

isoparametric elements for both domain fluid elements and for the absorbing boundary elements; for all numerical experiments we used unstructured quadrilateral meshes.

We consider three different depths of immersion, three angles of incidence (α=90° (vertically propagating wave), 45°, and a grazing angle of 5°), and both semi-circular and semi-elliptical boundaries. Table 1 summarizes for all cases the associated computational cost in terms of degrees-of-freedom.

Figs. 7–9 depict the amplitude of the scattered pressure field as computed at various points on the cylindrical scatterer's boundary (denoted in the plots by the polar angle θ). Both exact and approximate solutions are shown; the latter correspond to a semi-circular boundary ($\eta = 1$), and a semi-elliptical boundary ($\eta = 2$). Clearly, there is excellent agreement between the exact and circular-boundary cases; the agreement between the exact and the elliptical boundary is also quite satisfactory in all cases. We observe the greatest deviation from the exact solution in the case of the elliptical boundary (η=2) when the wave impinges at the grazing angle (Fig. 9). We remark though, that the use of the semi-elliptical geometries has allowed for considerable computational savings over the semi-circular boundaries; referring to Table 1, the savings, again in terms of degrees-of-freedom, are of the order of 60%. We further remark that the accuracy of both boundaries at the low-frequency end is also quite satisfactory.

Whereas Figs. 7–9 depict the response point-wise, in Fig. 10 we compare the numerical solution against the exact for the distribution of the scattered pressure amplitude along both the scatterer's boundary (Γ), and the absorbing boundary (Γ_a) for a single scattering case (angle of incidence $\alpha = 45°$, $ka = 1$). Notice again that the agreement is quite satisfactory.

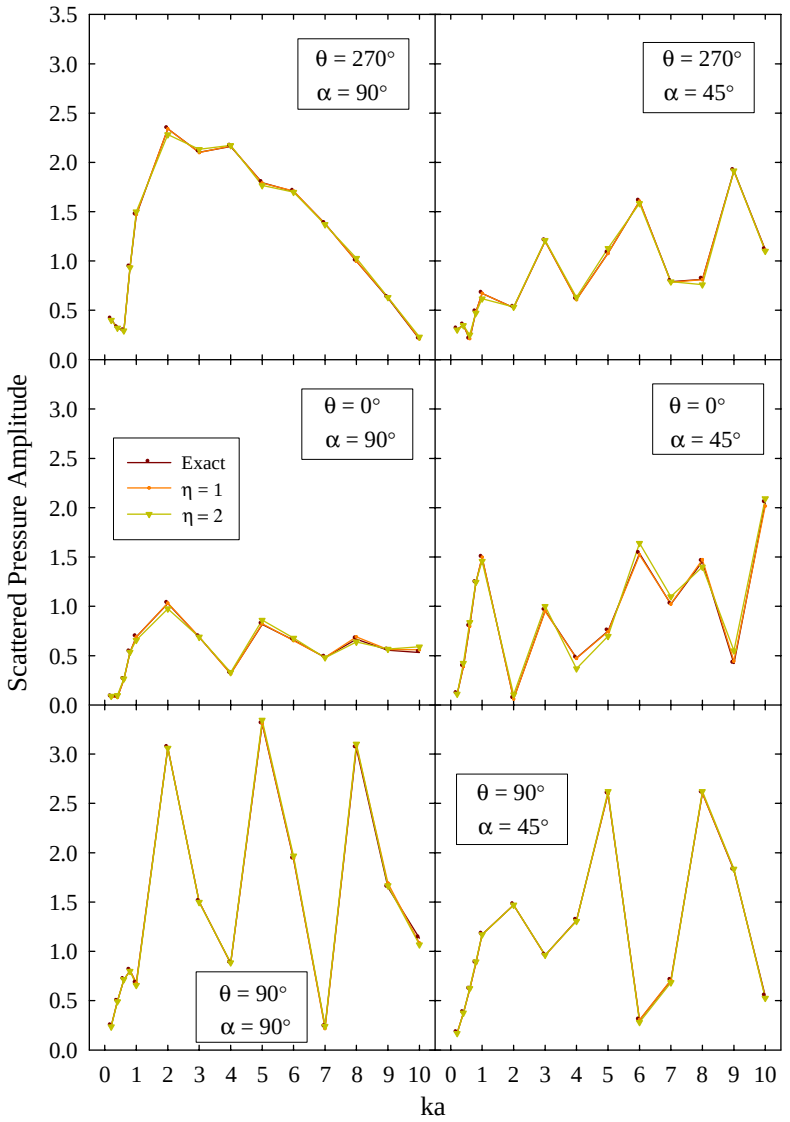

Fig. 7. Scattered pressure amplitude for a circular cylindrical scatterer; depth of immersion $d/2a = 2.0$; $s_M = 4.0a$.

Fig. 11 depicts a relative error measure E on the scatterer's boundary using L_2-norms for various ratios η and for a single immersion depth $d/2a = 2.0$ and angle of incidence $\alpha = 45°$. The error is defined as

$$E = \frac{[\int_\Gamma \| p_{ex} - p_{app} \|^2 \, d\Gamma]^{1/2}}{[\int_\Gamma \| p_{ex} \|^2 \, d\Gamma]^{1/2}} \times 100\%, \tag{40}$$

where p_{ex} is the exact solution derived from (A.16), and p_{app} is the finite element solution obtained by solving (33). In all cases, it appears that the circular boundary outperforms the elliptical one at an

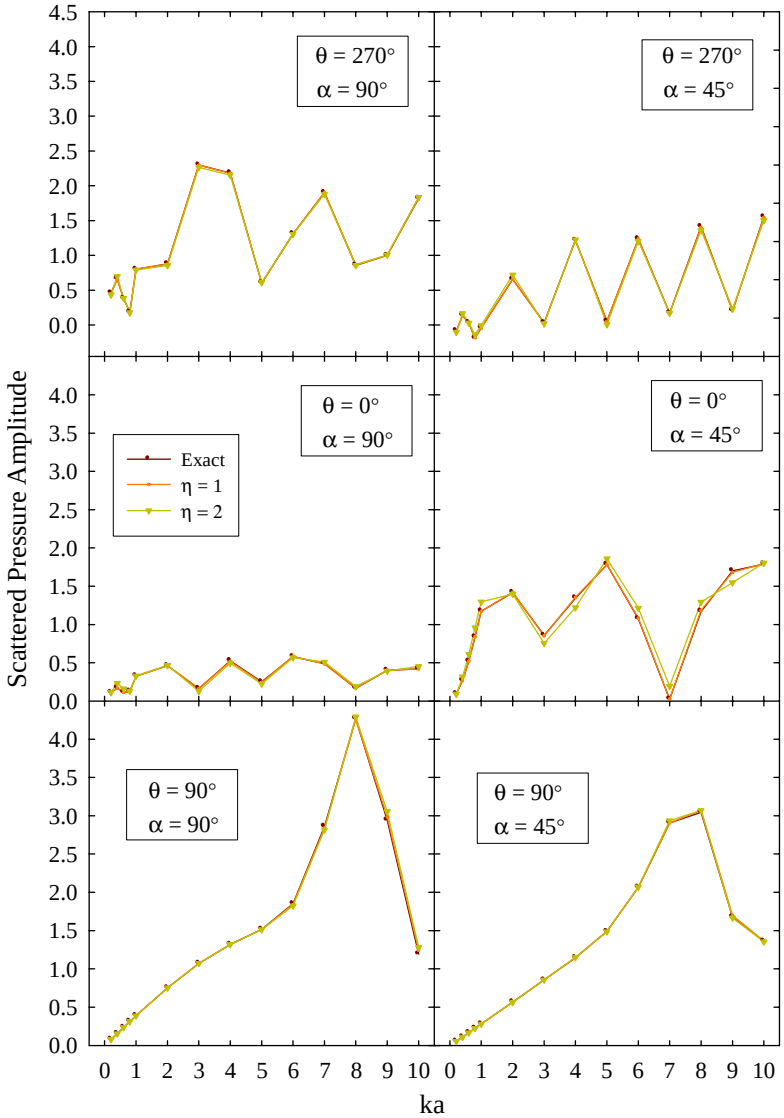

Fig. 8. Scattered pressure amplitude for a circular cylindrical scatterer; depth of immersion $d/2a = 1.2$; $s_M = 3.0a$.

increased computational cost. We remark however that the error levels for the elliptical boundaries (e.g. $\eta = 1.5$), are still quite satisfactory.

4.2. Cigar-shaped scatterer

To illustrate the applicability of the boundaries and the corresponding absorbing finite elements to problems of practical interest, we consider next an elongated cigar-shaped scatterer (Fig. 12),

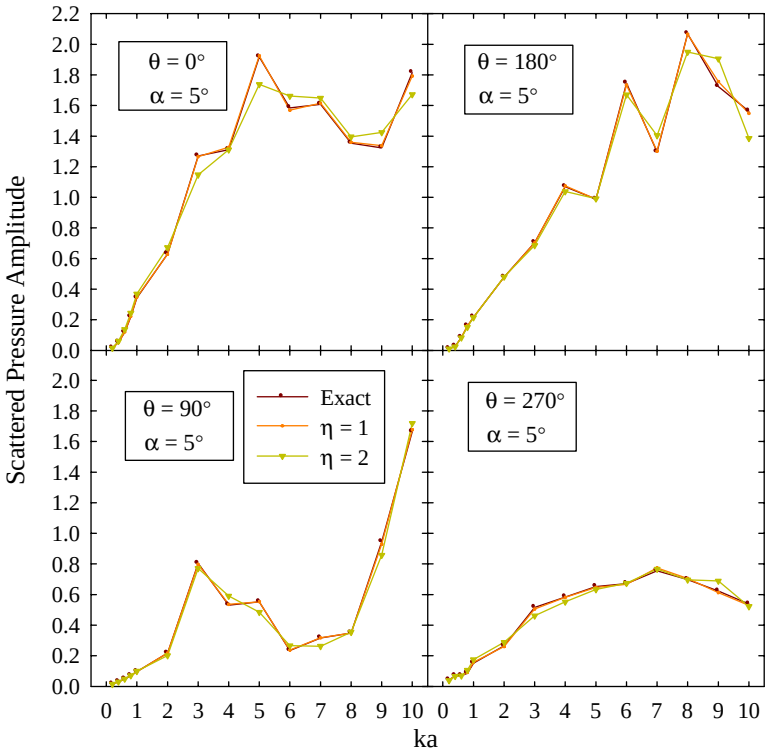

Fig. 9. Scattered pressure amplitude for a circular cylindrical scatterer; depth of immersion $d/2a = 1.5$; $s_M = 3.0a$.

for which the semi-elliptical boundary offers tighter circumscription, and therefore the potential for increased computational gains.

Since there is no exact solution in this case, we obtain a reference solution to compare against by using a semi-circular absorbing boundary with a radius of $22a$ endowed with the second-order condition. Table 2 summarizes the number of degrees-of-freedom used for each of the four cases for which we computed the response. The typical mesh element metric is $0.25a$. Fig. 13 depicts the distribution of the real and imaginary parts of the scattered field on the cigar-shaped scatterer's boundary for two frequencies ($ka = 1$ and $ka = 3$) and for a single incidence angle of 45°. The agreement between the exact and all approximate solutions is excellent. Notice though (Table 2) that, for comparable accuracy, the computational cost associated with $\eta = 2$ is less than half that of the semi-circular boundary.

To illustrate the applicability of the absorbing elements to transient simulations, Fig. 14 pertains to a direct time-domain solution of (33) for the scattered pressure field due to the insonification of the cigar-shaped scatterer by a traveling plane wave. We use the implicit trapezoidal rule to integrate in time the semi-discrete form (33) with a time-step $\Delta t\, c/a = 0.1$; the time signal for the plane wave is given by a finite-duration modified Ricker pulse with a central dimensionless frequency of 1 (see [30] for details). Again, as seen from Fig. 14 the agreement between the reference solution and the various elliptical boundaries at discrete points on the surface is excellent.

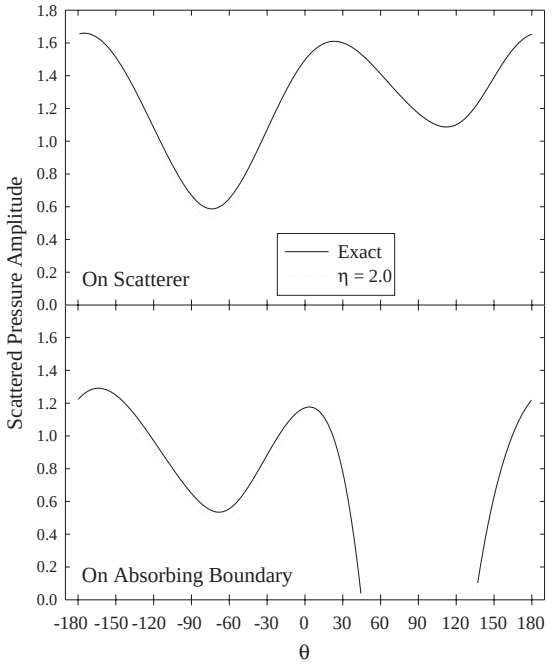

Fig. 10. Distribution of scattered pressure amplitude for a circular cylindrical scatterer; depth of immersion $d/2a = 1.2$; $s_M = 3.0a$; $\alpha = 45°$, $ka = 1$.

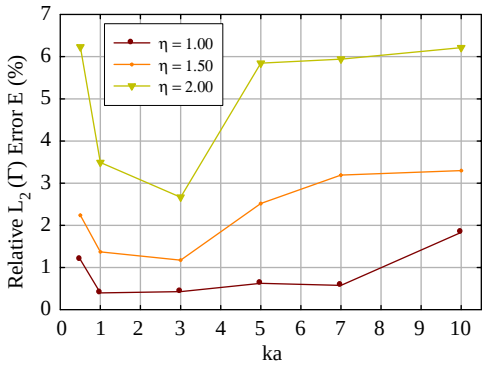

Fig. 11. Relative $L_2(\Gamma)$ error E (in percent) for elliptical and circular boundaries; depth of immersion $d/2a = 2.0$.

5. Conclusions

In this paper we discussed an efficient methodology for resolving scattered or total pressure fields arising in the numerical modeling of near-surface scatterers submerged in an acoustic half-plane. The primary objectives of this article were: (a) to provide the theoretical basis for extending full-plane conditions to the half-plane using the method of images; and (b) to demonstrate the significant

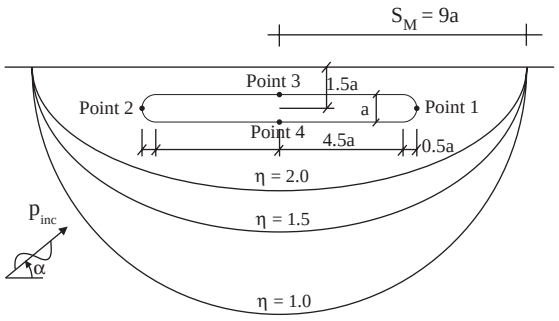

Fig. 12. Model of a rigid cigar-shaped scatterer in a half-plane surrounded by various elliptical absorbing boundaries.

Table 2
Computational cost in terms of the total number of degrees-of-freedom per case for the cigar-shaped scatterer

Semi-axes ratio $\eta = s_M/s_m$	Total DOF
2.0	23 798
1.5	32 914
1.0	52 174
Reference	321 008

computational gains that are attainable, at no or minimal loss of accuracy, when elliptically-shaped boundaries are adopted over their circular counterparts for the truncation of the semi-infinite extent of the physical domain. Borrowing from full-plane developments of earlier works, we have shown that the ease by which second-order conditions can be incorporated into existing finite element codes extends to the half-plane case as well.

Acknowledgements

We wish to thank the reviewers for their helpful suggestions.

Appendix A. The exact solution

In order to compare the numerical results obtained using the outlined approach against exact solutions to canonical problems, we provide next the solution to the scattering problem arising when a time-harmonic plane wave insonifies a near-surface rigid circular cylindrical scatterer. While the exact solution to this problem appears not to be readily available in the literature, a closely related solution that follows similar lines, albeit for the more complex case of an elastic cylinder, can be found in [31].

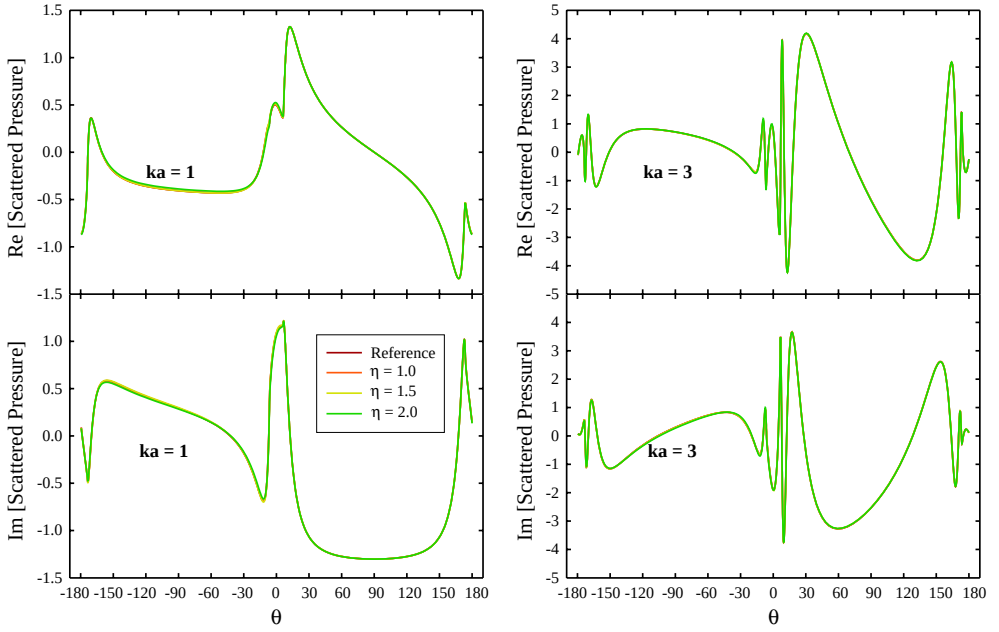

Fig. 13. Real and imaginary parts of the scattered pressure on the cigar-shaped scatterer (Fig. 12) for $ka = 1$ and $ka = 3$; $\alpha = 45^\circ$.

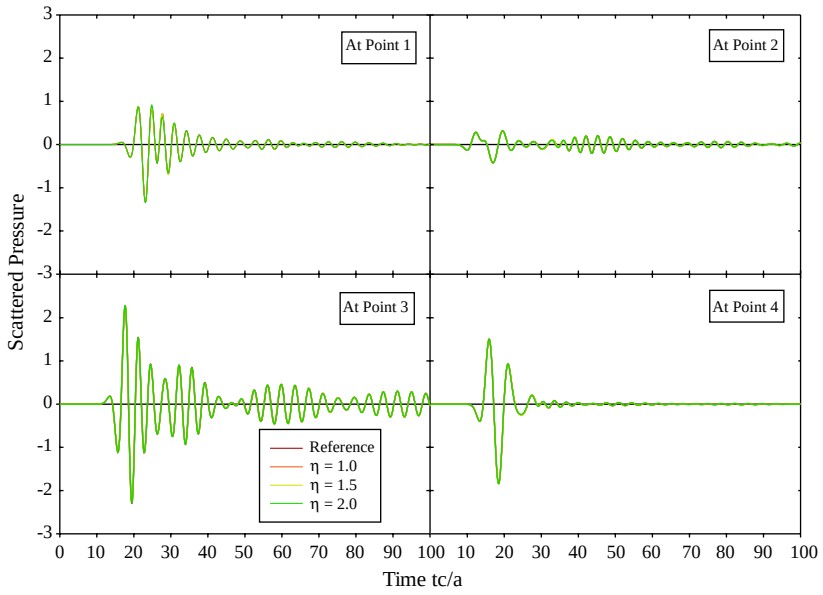

Fig. 14. Scattered pressure trace at various points on the surface of the cigar-shaped scatterer (Fig. 12); transient response to a traveling plane wave; various boundaries; $\alpha = 45^\circ$.

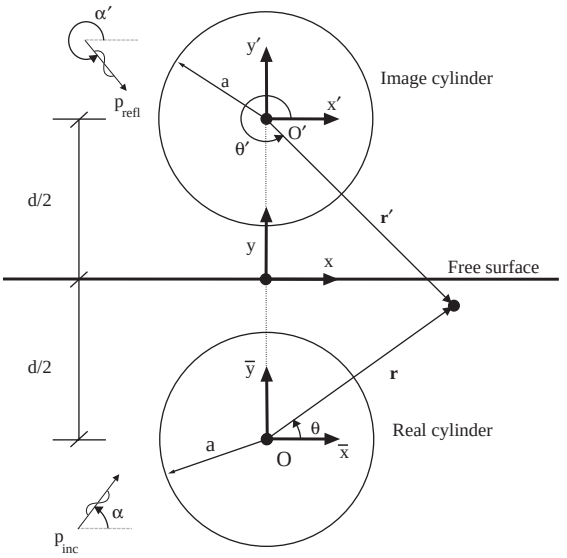

Fig. 15. Geometry of a rigid circular scatterer in a half-plane; real and image scatterers.

Accordingly, we resort again to the method of images in conjunction with an addition theorem for cylindrical wave functions. We consider the geometry shown in Fig. 15. The image and real scatterers are separated by a distance d between their centers O' and O, respectively.

We consider an incident time-harmonic plane wave p_{inc} impinging at an angle of incidence α with respect to the positive x-axis.

$$p_{\text{inc}}(x, y, t) = \mathrm{e}^{\mathrm{i}k(x\cos\alpha + y\sin\alpha)}\mathrm{e}^{-\mathrm{i}\omega t}. \tag{A.1}$$

Similarly, the image incident, or free-field reflected wave, p_{refl}, is

$$p_{\text{refl}}(x, y, t) = -\mathrm{e}^{\mathrm{i}k(x\cos\alpha - y\sin\alpha)}\mathrm{e}^{-\mathrm{i}\omega t}, \tag{A.2}$$

where k denotes wavenumber ($k = \omega/c$). Using polar coordinates (r, θ) for the system that has origin at O (Fig. 15), and the following transformations:

$$x = \bar{x} = r\cos\theta, \quad y = \bar{y} - \frac{d}{2} = r\sin\theta - \frac{d}{2}, \tag{A.3}$$

the real and image incident waves (A.1) and (A.2), respectively, can be written as (we drop the $\mathrm{e}^{-\mathrm{i}\omega t}$ dependence from all subsequent expressions):

$$p_{\text{inc}}(r, \theta) = \mathrm{e}^{-\mathrm{i}k(d/2)\sin\alpha}\ \mathrm{e}^{\mathrm{i}kr\cos(\theta-\alpha)}, \tag{A.4}$$

$$p_{\text{refl}}(r, \theta) = -\mathrm{e}^{\mathrm{i}k\,(d/2)\sin\alpha}\ \mathrm{e}^{\mathrm{i}kr\cos(\theta+\alpha)}. \tag{A.5}$$

Using a Jacobi–Auger expansion [32], Eqs. (A.4)–(A.5) can be further re-written in terms of series of cylindrical Bessel functions, as

$$p_{\text{inc}}(r,\theta) = \mathrm{e}^{-\mathrm{i}k(d/2)\sin\alpha}\,\mathrm{e}^{\mathrm{i}kr\cos(\theta-\alpha)}$$

$$= \mathrm{e}^{-\mathrm{i}k(d/2)\sin\alpha}\sum_{n=-\infty}^{\infty} i^n J_n(kr)\,\mathrm{e}^{\mathrm{i}n\theta}\mathrm{e}^{-\mathrm{i}n\alpha}, \tag{A.6}$$

$$p_{\text{refl}}(r,\theta) = -\mathrm{e}^{\mathrm{i}k(d/2)\sin\alpha}\,\mathrm{e}^{\mathrm{i}kr\cos(\theta+\alpha)}$$

$$= -\,\mathrm{e}^{\mathrm{i}k(d/2)\sin\alpha}\sum_{n=-\infty}^{\infty} i^n J_n(kr)\,\mathrm{e}^{\mathrm{i}n\theta}\mathrm{e}^{\mathrm{i}n\alpha}. \tag{A.7}$$

We next define two additional wavefields, namely, the scattered field due to the real cylinder $p_{\text{sc}}^{\text{real}}$ (if the real cylinder alone were occupying the full-plane and were insonified by p_{inc}), and the scattered field due to the image cylinder $p_{\text{sc}}^{\text{image}}$ (again, if the image cylinder alone were occupying the full-plane and were insonified by p_{refl}). Accordingly

$$p_{\text{sc}}^{\text{real}}(r,\theta) = \sum_{n=-\infty}^{\infty} a_n H_n^{(1)}(kr)\mathrm{e}^{\mathrm{i}n\theta}, \tag{A.8}$$

$$p_{\text{sc}}^{\text{image}}(r',\theta') = \sum_{n=-\infty}^{\infty} b_n H_n^{(1)}(kr')\mathrm{e}^{\mathrm{i}n\theta'}. \tag{A.9}$$

Both scattered fields above have been obtained as solutions to the Helmholtz equation written in the polar coordinate systems with origins at O and O', respectively. Clearly, the sum of all four fields is equal to the total pressure field for the half-plane problem, i.e.,

$$p_{\text{tot}} = p_{\text{inc}} + p_{\text{refl}} + p_{\text{sc}}^{\text{real}} + p_{\text{sc}}^{\text{image}}. \tag{A.10}$$

Since on the free surface Γ_{f}, the total field (A.10) must vanish (see (21)), and, by construction, the sum of the real and image incident fields also vanishes on Γ_{f} (see (23)), there results

$$p_{\text{sc}}^{\text{real}}(r,\theta) + p_{\text{sc}}^{\text{image}}(r',\theta') = 0 \quad \text{on } \Gamma_{\text{f}}. \tag{A.11}$$

Using $r' \equiv r$ and $\theta' \equiv 2\pi - \theta$ on Γ_{f}, (A.11) becomes

$$p_{\text{sc}}^{\text{real}}(r,\theta) + p_{\text{sc}}^{\text{image}}(r,2\pi-\theta)$$

$$= \sum_{n=-\infty}^{\infty} a_n H_n^{(1)}(kr)\mathrm{e}^{\mathrm{i}n\theta} + \sum_{n=-\infty}^{\infty} b_n H_n^{(1)}(kr)\mathrm{e}^{\mathrm{i}n(2\pi-\theta)}$$

$$= \sum_{n=-\infty}^{\infty} a_n H_n^{(1)}(kr)\mathrm{e}^{\mathrm{i}n\theta} + \sum_{m=\infty}^{-\infty} b_{-m} H_{-m}^{(1)}(kr)\mathrm{e}^{\mathrm{i}m\theta}$$

$$= \sum_{n=-\infty}^{\infty} a_n H_n^{(1)}(kr)\mathrm{e}^{\mathrm{i}n\theta} + \sum_{m=-\infty}^{\infty} b_{-m}\mathrm{e}^{m\pi\mathrm{i}} H_m^{(1)}(kr)\mathrm{e}^{\mathrm{i}m\theta}$$

$$= \sum_{n=-\infty}^{\infty} a_n H_n^{(1)}(kr)\mathrm{e}^{\mathrm{i}n\theta} + \sum_{n=-\infty}^{\infty} b_{-n}(-1)^n H_n^{(1)}(kr)\mathrm{e}^{\mathrm{i}n\theta}$$

$$= \sum_{n=-\infty}^{\infty} [a_n + (-1)^n b_{-n}] H_n^{(1)}(kr)\mathrm{e}^{\mathrm{i}n\theta} = 0. \tag{A.12}$$

Therefore,

$$b_{-n} = (-1)^{n+1} a_n. \tag{A.13}$$

Next, we use an addition theorem for cylindrical waves [32] to transform $p_{\mathrm{sc}}^{\mathrm{image}}$ (A.9) to the same coordinate system (origin at O) as $p_{\mathrm{sc}}^{\mathrm{real}}$ (A.8). Accordingly

$$H_n^{(1)}(kr')\mathrm{e}^{\mathrm{i}n\theta'} = \sum_{m=-\infty}^{\infty} \left\{ \begin{array}{ll} H_{n-m}^{(1)}(kd)\, J_m(kr)\, \mathrm{e}^{\mathrm{i}[(n-m)3\pi/2+m\theta]}, & r \leqslant d \\ J_m(kd)\, H_{n-m}^{(1)}(kr)\, \mathrm{e}^{\mathrm{i}[m3\pi/2+(n-m)\theta]}, & r \geqslant d \end{array} \right\}. \tag{A.14}$$

Using (A.13), (A.14), after manipulation of the series indices, becomes:

$$p_{\mathrm{sc}}^{\mathrm{image}}(r,\theta) = \sum_{n=-\infty}^{\infty} \left\{ (-1)^{n+1} i^n \begin{array}{c} J_n(kr) \\ H_n^{(1)}(kr) \end{array} \mathrm{e}^{\mathrm{i}n\theta} \left[\sum_{m=-\infty}^{\infty} a_m i^m \begin{array}{c} H_{m+n}^{(1)}(kd) \\ J_{m+n}(kd) \end{array} \right], \begin{array}{l} r \leqslant d \\ r \geqslant d \end{array} \right\}. \tag{A.15}$$

Substituting (A.6)–(A.8) and (A.15) into (A.10), the total pressure p_{tot} becomes

$$\begin{aligned} p_{\mathrm{tot}}(r,\theta) &= p_{\mathrm{inc}}(r,\theta) + p_{\mathrm{refl}}(r,\theta) + p_{\mathrm{sc}}^{\mathrm{real}}(r,\theta) + p_{\mathrm{sc}}^{\mathrm{image}}(r,\theta) \\ &= \sum_{n=-\infty}^{\infty} \Bigg[\mathrm{e}^{-\mathrm{i}k(d/2)\sin\alpha} i^n \mathrm{e}^{-\mathrm{i}n\alpha} J_n(kr) \\ &\quad - \mathrm{e}^{\mathrm{i}k(d/2)\sin\alpha} i^n \mathrm{e}^{\mathrm{i}n\alpha} J_n(kr) + a_n H_n^{(1)}(kr) + (-1)^{n+1} i^n \\ &\quad \times \begin{array}{c} J_n(kr) \\ H_n^{(1)}(kr) \end{array} \mathrm{e}^{\mathrm{i}n\theta} \left[\sum_{m=-\infty}^{\infty} a_m i^m \begin{array}{c} H_{m+n}^{(1)}(kd) \\ J_{m+n}(kd) \end{array} \right] \Bigg], \begin{array}{l} r \leqslant d \\ r \geqslant d. \end{array} \end{aligned} \tag{A.16}$$

Eq. (A.16) provides the solution for the total pressure anywhere within the half-plane ($y \leqslant 0$). All that remains is to compute the unknown series coefficients a_n. To this end, we consider the boundary condition on the surface of the sound-hard real cylinder, i.e., we set $\partial p_{\mathrm{tot}}/\partial r|_{r=a} = 0$. There results:

$$-\frac{H_n^{'(1)}(ka)}{i^n J_n'(ka)} a_n + (-1)^n \sum_{m=-\infty}^{\infty} a_m i^m H_{m+n}^{(1)}(kd)$$

$$= -2i \sin\left(k\frac{d}{2} \sin\alpha + n\alpha \right), \quad \forall n. \tag{A.17}$$

Eq. (A.17) represents an infinite system of algebraic equations for the determination of the unknown coefficients a_n involved in the series (A.16). Once the coefficients are determined, the total pressure

is given by (A.16), and the total scattered field by

$$p_{\mathrm{sc}}(r,\theta) = p_{\mathrm{tot}}(r,\theta) - p_{\mathrm{inc}}(r,\theta). \tag{A.18}$$

Appendix B. Implementational details

In implementing the discrete problem discussed in Section 3 we used standard isoparametric elements. We discuss the details pertaining to the various integrals of the absorbing element matrices in (38) and (39) using, without loss of generality, linear approximations. Accordingly, for any element e of the discretized artificial boundary, we used the standard map:

$$x = \psi^{\mathrm{T}}(\xi)\boldsymbol{x}^e, \quad y = \psi^{\mathrm{T}}(\xi)\boldsymbol{y}^e, \tag{B.1}$$

where $\boldsymbol{x}^e$ and $\boldsymbol{y}^e$ denote the nodal coordinates of element e in a global Cartesian coordinate system (x, y), and ξ denotes the local coordinate, with $\xi \in (-1, 1)$. For a linear approximation:

$$\psi(\xi) = \frac{1}{2}\begin{bmatrix} 1-\xi \\ 1+\xi \end{bmatrix}, \quad \psi_\xi(\xi) = \frac{1}{2}\begin{bmatrix} -1 \\ 1 \end{bmatrix}. \tag{B.2}$$

Then,

$$\mathrm{d}\lambda^e = \sqrt{x_\xi^2 + y_\xi^2}\,\mathrm{d}\xi = \sqrt{(\psi_\xi^{\mathrm{T}}\boldsymbol{x}^e)^2 + (\psi_\xi^{\mathrm{T}}\boldsymbol{y}^e)^2}\,\mathrm{d}\xi = j_\xi\,\mathrm{d}\xi, \tag{B.3}$$

$$\psi_\lambda(\xi) = \frac{1}{j_\xi}\begin{bmatrix} -\frac{1}{2} \\ \frac{1}{2} \end{bmatrix}. \tag{B.4}$$

Finally, in all expressions where the curvature κ appears, we used its exact value, which for an ellipse with semi-axes s_{M} and s_{m} reduces to:

$$\kappa(x,y) = -s_{\mathrm{M}}s_{\mathrm{m}}/(s_{\mathrm{m}}^2/s_{\mathrm{M}}^2 x^2 + s_{\mathrm{M}}^2/s_{\mathrm{m}}^2 y^2)^{3/2}. \tag{B.5}$$

References

[1] J.B. Keller, D. Givoli, Exact non-reflecting boundary conditions, J. Comput. Phys. 82 (1989) 172–192.
[2] D. Givoli, Non-reflecting boundary conditions: a review, J. Comput. Phys. 94 (1) (1991) 1–29.
[3] E. Kausel, J.L. Tassoulas, Transmitting boundaries: a closed-form comparison, Bull. Seismol. Soc. Amer. 71 (1981) 143–159.
[4] J.P. Wolf, A comparison of time-domain transmitting boundaries, Earthquake Eng. Struc. Dyn. 14 (1986) 655–673.
[5] E. Kausel, Local transmitting boundaries, ASCE J. Eng. Mech. 114 (6) (1988) 1011–1027.
[6] S.V. Tsynkov, Numerical solution of problems on unbounded domains. A review, Appl. Numer. Math. 27 (1998) 465–532.
[7] B. Engquist, A. Majda, Absorbing boundary conditions for the numerical simulation of waves, Math. Comp. 31 (1977) 629–651.
[8] B. Engquist, A. Majda, Radiation boundary conditions for acoustic and elastic wave calculations, Comm. Pure Appl. Math. 32 (1979) 313–357.
[9] A. Bayliss, E. Turkel, Radiation boundary conditions for wave-like equations, Comm. Pure Appl. Math. 33 (1980) 707–725.

[10] A. Bayliss, E. Turkel, Far field boundary conditions for compressible flows, J. Comput. Phys. 48 (1982) 182–199.
[11] A. Bayliss, M. Gunzburger, E. Turkel, Boundary conditions for the numerical solution of elliptic equations in exterior regions, SIAM J. Appl. Math. 42 (2) (1982) 430–451.
[12] G.A. Kriegsmann, A. Taflove, K.R. Umashankar, A new formulation of electromagnetic wave scattering using an on-surface radiation boundary condition approach, IEEE Trans. Antennas Propagation AP-35 (2) (1987) 153–160.
[13] D.S. Jones, An approximate boundary condition in acoustics, J. Sound Vibration 121 (1) (1988) 37–45.
[14] A. Khebir, O. Ramahi, R. Mittra, An efficient partial differential equation technique for solving the problem of scattering by objects of arbitrary shape, Microwave Opt. Tech. Lett. 2 (1989) 229–233.
[15] C.F. Lee, R.T. Shin, J.A. Kong, B.J. McCartin, Absorbing boundary conditions on circular and elliptical boundaries, J. Electromagn. Waves Appl. 4 (10) (1990) 945–962.
[16] Y. Li, Z.J. Cendes, Modal expansion absorbing boundary conditions for two-dimensional electromagnetic scattering, IEEE Trans. Magn. 29 (1993) 1835–1838.
[17] B. Stupfel, Absorbing boundary conditions on arbitrary boundaries for the scalar and wave equations, IEEE Trans. Antennas Propagation 42 (6) (1994) 773–780.
[18] M.J. Grote, J.B. Keller, On nonreflecting boundary conditions, J. Comput. Phys. 122 (1995) 231–243.
[19] X. Antoine, H. Barucq, A. Bendali, Bayliss-Turkel-like radiation conditions on surfaces of arbitrary shape, J. Math. Anal. Appl. 229 (1999) 184–211.
[20] A. Barry, J. Bielak, R.C. MacCamy, On absorbing boundary conditions for wave propagation, J. Comput. Phys. 79 (1988) 449–468.
[21] L.F. Kallivokas, J. Bielak, R.C. MacCamy, Symmetric local absorbing boundaries in time and space, ASCE J. Eng. Mech. 117 (9) (1991) 2027–2048.
[22] L.F. Kallivokas, J. Bielak, R.C. MacCamy, Absorbing boundary conditions of arbitrary shape for the three-dimensional wave equation, in: IUTAM Symposium on Computational Methods for Unbounded Domains, Kluwer Academic Publishers, Boulder, CO, July 1997, pp. 221–228.
[23] L.F. Kallivokas, J. Bielak, A simple impedance-infinite element for the finite element solution of the three-dimensional wave equation in unbounded domains, Comput. Methods Appl. Mech. Engng. 147 (1997) 235–262.
[24] R. Djellouli, C. Farhat, A. Macedo, R. Tezaur, Finite element solution of two-dimensional acoustic scattering problems using arbitrarily shaped convex artificial boundaries, J. Comput. Acoust. 8 (1) (2000) 81–99.
[25] S.K. Bhattacharyya, S. Sathyapal, C.P. Vendhan, Absorbing boundary condition on elliptic boundary for the finite element analysis of water wave diffraction by large elongated bodies, Internat. J. Numer. Meth. Fluids 37 (2001) 249–277.
[26] D.B. Meade, G.W. Slade, A.F. Peterson, K.J. Webb, Comparison of local radiation boundary conditions for the scalar Helmholtz equation with general boundary shape, IEEE Trans. Antennas and Propagation 43 (1995) 1–5.
[27] B. Lichtenberg, K.J. Webb, D.B. Meade, A.F. Peterson, Comparison of two-dimensional conformal local radiation boundary conditions, Electromagnetics 16 (1996) 359–384.
[28] L.F. Kallivokas, A. Tsikas, J. Bielak, On transient three-dimensional absorbing boundary conditions for the modeling of acoustic scattering from near-surface obstacles, J. Comput. Acoust. 5 (1) (1997) 117–136.
[29] J. Bielak, L.F. Kallivokas, J. Xu, R. Monopoli, Finite element absorbing boundary for the wave equation in a half-plane with an application to engineering seismology, Proceedings of the Third International Conference on Mathematical and Numerical Aspects of Wave Propagation (INRIA-SIAM), 489–498, Juan-les-Pins, France, April 1995.
[30] L.F. Kallivokas, S. Lee, Local high-order absorbing boundaries of elliptical shape for scalar waves, Comput. Meth. Appl. Mech. Eng. (2004), accepted.
[31] V.W. Lee, M.D. Trifunac, Response of tunnels to incident SH-waves, J. Eng. Mech. Div. ASCE 105 (1979) 643–659.
[32] A. Ivanov Ye, Diffraction of electromagnetic waves on two bodies, NASA translation of Difraktsiya elektromagnitnykh voln na dvukh telakh, Nauka i Tekhnika Press, Minsk, 1968.